In vivo three-dimensional photoacoustic imaging based on a clinical matrix array ultrasound probe

Yu Wang
Todd N. Erpelding
Ladislav Jankovic
Zijian Guo
Jean-Luc Robert
Guillaume David
Lihong V. Wang

In vivo three-dimensional photoacoustic imaging based on a clinical matrix array ultrasound probe

Yu Wang,[a*] Todd N. Erpelding,[b*] Ladislav Jankovic,[b] Zijian Guo,[a] Jean-Luc Robert,[b] Guillaume David,[b] and Lihong V. Wang[a]
[a]Washington University in St. Louis, Department of Biomedical Engineering, Optical Imaging Laboratory, 1 Brookings Drive, St. Louis, Missouri 63130
[b]Philips Research North America, 345 Scarborough Road, Briarcliff Manor, New York 10510

Abstract. We present an integrated photoacoustic and ultrasonic three-dimensional (3-D) volumetric imaging system based on a two-dimensional (2-D) matrix array ultrasound probe. A wavelength-tunable dye laser pumped by a *Q*-switched Nd:YAG laser serves as the light source and a modified commercial ultrasound imaging system (iU22, Philips Healthcare) with a 2-D array transducer (X7-2, Philips Healthcare) detects both the pulse-echo ultrasound and photoacoustic signals. A multichannel data acquisition system acquires the RF channel data. The imaging system enables rendering of co-registered 3-D ultrasound and photoacoustic images without mechanical scanning. The resolution along the azimuth, elevation, and axial direction are measured to be 0.69, 0.90 and 0.84 mm for photoacoustic imaging. *In vivo* 3-D photoacoustic mapping of the sentinel lymph node was demonstrated in a rat model using methylene blue dye. These results highlight the clinical potential of 3-D PA imaging for identification of sentinel lymph nodes for cancer staging in humans. © *2012 Society of Photo-Optical Instrumentation Engineers (SPIE).* [DOI: 10.1117/1.JBO.17.6.061208]

Keywords: photoacoustic imaging; ultrasound imaging; three-dimensional imaging; sentinel lymph node.

Paper 11549SSP received Sep. 30, 2011; revised manuscript received Dec. 14, 2011; accepted for publication Dec. 19, 2011.; published online May 7, 2012.

1 Introduction

Photoacoustic (PA) imaging, combining optical absorption contrast with fine ultrasonic resolution, enables deeply penetrating *in vivo* imaging.[1] Pure optical imaging modalities (e.g., optical coherence tomography and diffuse optical tomography) encounter a fundamental limitation of either penetration or spatial resolution at depths beyond one optical transport mean free path (∼1 mm) due to strong light scattering by biological tissue. PA imaging, however, provides a high ultrasonic spatial resolution for deep imaging by utilizing ultrasonic detection of the PA wave generated by absorbed diffuse light.[2,3] Deep PA imaging has been used to image both biological structure (e.g., internal organs,[4,5] and sentinel lymph nodes[6]) and function (e.g., tumor hypoxia,[7] and brain oxygenation[8,9]).

The ability of PA imaging (PA microscopy and PA computed tomography[1]) systems to render three-dimensional (3-D) volumetric images relies on recording the PA time-of-flight signals on a two-dimensional (2-D) surface facing the photoacoustic source, light-absorbing chromophores. Due to the system cost and complexity when employing a large number of data acquisition (DAQ) channels, currently most PA imaging systems utilize a single-element ultrasound (US) transducer[7–10] or a one-dimensional (1-D) array US probe.[4–6,11] Mechanical scanning of the US probe required by these systems to form 3-D PA images limits the volumetric imaging frame rate. Thus, 3-D PA imaging systems using 2-D array US probes have been recently studied. Khuri-Yakub et al. have fabricated a 2-D capacitive micromachined ultrasonic transducer (CMUT)

with 16 × 16 elements (pitch size, 250 μm) for PA and US imaging.[12] Mechanical scanning was needed to form a large detection aperture to improve the image quality. Zhu et al. have developed a 2-D array US transducer with 10 × 128 elements for US and PA characterization of ovarian tissue.[13] This imaging system is limited in the beam steering angle and elevational resolution. Van Leeuwen et al. have used a polyvinylidene fluoride (PVDF) based hydrophone matrix consisting of 590 elements in a research prototype system for breast cancer detection.[14,15] The large detector element size of 2 × 2 mm^2 limits the spatial resolution of the imaging system. We developed a 3-D PA imaging system based on a clinical 2-D matrix array US probe with the modified US scanner to enable 3-D PA and US imaging without mechanical scanning. Optical fiber bundles for light delivery were physically integrated with the matrix array US probe (2500 elements), while the capability of real-time 3-D US imaging was maintained.

Sentinel lymph node biopsy (SLNB) is an emerging method for axillary lymph node staging in clinically node-negative breast cancer patients.[16] The current SLNB technique requires an injection of radioactive colloids and blue dyes for identification of sentinel lymph nodes (SLNs). Following invasive visual confirmation, SLNs are surgically resected for pathological examination of the excised tissue. The invasive surgical procedure leads to potential postoperative complications, such as lymphedema, seroma formation, sensory nerve injury, and limitation in the range of motion.[17] Therefore, PA imaging has been proposed as an alternative method of noninvasive SLN identification and photoacoustically-guided minimally invasive fine-needle aspiration biopsy.[18] Noninvasive mapping of SLNs using PA imaging of the injected blue dye accumulated

---

*Contributed equally to this paper.

Address all correspondence to: Lihong V. Wang, Washington University, Department of Biomedical Engineering, St. Louis, Missouri 63130. Tel: +314 9356152; Fax: +314 9357448; E-mail: lhwang@seas.wustl.edu.

in the SLNs would enable targeted needle biopsy. Moreover, PA imaging features lower speckle signal from the background biological tissue than US imaging.[2]

Our group previously reported a modified clinical US scanner using a linear US array for clinical translation of PA sentinel lymph node mapping.[6] In this report, we evaluated the performance of the matrix US array based multi-modal 3-D imaging system using a resolution phantom, and demonstrated 3-D *in vivo* PA SLN mapping in a rat model.

2 Methods and Materials

2.1 Imaging System Description

The PA imaging system adapted from a clinical US scanner (iU22, Philips Healthcare, Andover, MA) is shown in Fig. 1. The channel board architecture was modified to allow acquisition of the raw per-channel PA and US data. The dual-modality image data were transferred to a custom-built data acquisition (DAQ) system for image reconstruction and display. For 3-D PA and US imaging, we used the 2-D matrix array US probe (X7-2, Philips Healthcare) which has 2500 elements and a nominal bandwidth of 2 to 7 MHz. Each frame of the PA volumetric image requires 36 laser shots and takes 20 sec, limited by the current DAQ system performance. The DAQ system was synchronized with laser firings by an FPGA-based electronic board and digital delay generator (Stanford Research Systems, Sunnyvale, CA). A 3-D back-projection algorithm was implemented using Matlab (MathWorks Inc., Natick, MA) to reconstruct PA images.[19] The image reconstruction for one $2 \times 2 \times 2$ cm^3 volumetric image consisting of $100 \times 100 \times 400$ voxels took approximately 3 h on a 4-core central processing unit (CPU). Because the X7-2 array probe performs partial beamforming within the transducer to reduce the number of DAQ system channels needed for the large number of transducer elements, a novel proprietary algorithm reverses the partial beamforming process to recover raw PA channel data.

A wavelength tunable dye laser (PrecisionScan-P, Sirah, Kaarst, Germany), pumped by a Q-switched Nd:YAG laser (PRO-350-10, Spectra-Physics, Santa Clara, CA) serves as the light source for the PA imaging. The laser pulse is coupled to a fused end, bifurcated fiber bundle (LightGuideOptics, Rheinbach, Germany) integrated with the matrix array US probe. The laser emits pulses at a repetition rate of 10 Hz and pulse duration of 6.5 ns. An optical wavelength of 650 nm,
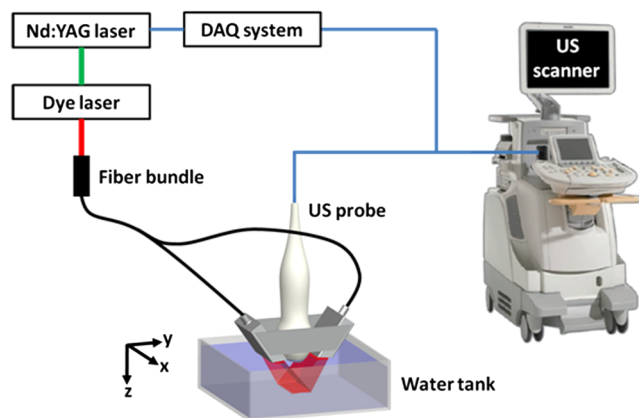
which is close to the peak absorption wavelength of methylene blue dye, was utilized for all the experiments. The light fluence on the skin was less than 10 mJ/cm^2, which is within the American National Standards Institute (ANSI) safety limits.[20]

2.2 Gelatin Phantom Preparation

To study the spatial resolution of the 3-D PA imaging system, an optically and acoustically transparent gelatin phantom (10% by weight) was prepared with a human hair embedded, which was placed parallel to the probe surface at a depth of ∼2 cm. A second gelatin phantom consisting of one white hair, one black hair, and a gelatin slab dyed with black ink was imaged to illustrate the complementary optical absorption and US scattering contrasts of PA and US imaging. A third phantom consisted of three hairs placed 10, 15, and 20 mm deep in a clear gelatin phantom. This phantom was designed to demonstrate 3-D volumetric PA imaging.

2.3 In Vivo 3-D PA Imaging of Rat SLNs

Sprague Dawley rats (∼200 g) were anesthetized using a mixture of ketamine (85 mg/kg) and xylazine (15 mg/kg). After hair depilation in the left axillary region, a series of PA and US images were collected before and after a 100 μL intradermal injection of 1% methylene blue dye (10 mg/mL, American Reget, Inc., Shirley, NY) into the left forepaw pad. The axillary region of the rat was imaged for 30 min following methylene blue injection. For US coupling, a water tank was applied between the US probe and the tissue surface during *in vivo* experiments. Axillary lymph nodes in the rat are approximately 2 mm below the skin surface. After imaging, animals were euthanized with an overdose of pentobarbital, and SLNs were dissected to confirm methylene blue dye uptake. Animal handling was performed according to the guidelines on the care and use of laboratory animals at Washington University in St. Louis.

3 Results

3.1 Gelatin Phantom Imaging

The resolution of the matrix array US probe was estimated using PA images of a human hair embedded within the gelatin. The hair is first imaged when placed along the azimuth direction of
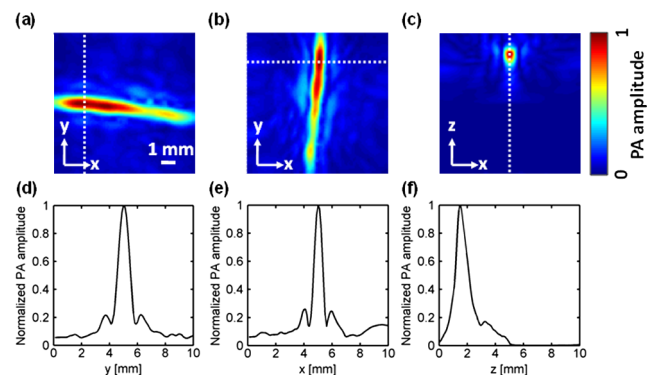

Fig. 2 PA MAP images of the hair positioned along the (a) azimuth and (b) elevation direction. (c) PA B-mode image of the hair positioned along the elevation direction. PA amplitude profiles crossing the human hair along the (d) elevation, (e) azimuth, and (f) axial directions, respectively. PA, photoacoustic; US, ultrasound; and DAQ, data acquisition.
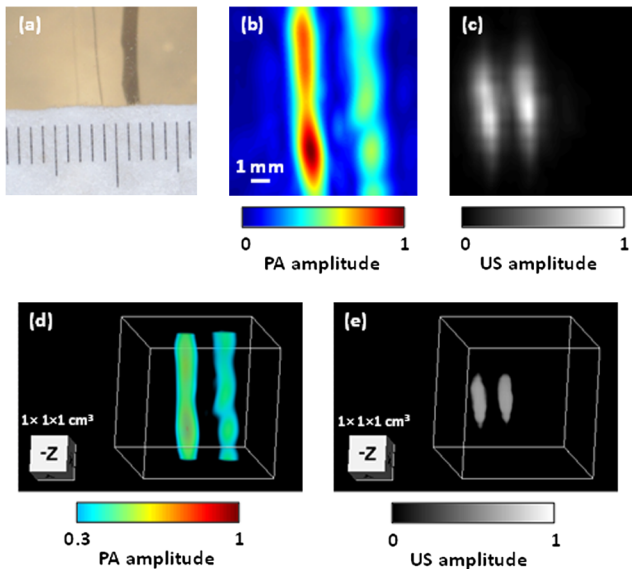

Fig. 1 Schematic of the integrated 3-D PA and US imaging system using a 2-D matrix array ultrasound probe.

Fig. 3 (a) Photograph of the gelatin phantom consisting of one white hair, one black hair, and a gelatin slab dyed with black ink. (b) PA MAP image showing the black hair and the ink dyed gelatin slab. (c) US MAP image showing the white hair and the black hair. (d) PA 3-D image. (e) US 3-D image. PA, photoacoustic; and US, ultrasound.

the probe and then imaged with the hair placed along the elevation direction. The PA maximum amplitude projection (MAP) images are formed by projecting the 3-D PA onto the surface plane of the probe. Figure 2(a) and 2(b) shows the PA MAP images of the hair positioned along the azimuth and elevation directions, respectively. Figure 1(c) displays the PA B-mode image of the hair positioned along the elevation direction. Figure 2(d)–2(f) displays the 1-D PA amplitude profiles crossing the hair along the elevation, azimuth, and axial directions as indicated by the dashed lines in Fig. 2(a)–2(c). We used the full width at half maximum of each 1-D PA amplitude profile to quantify the corresponding spatial resolution. At a depth of ∼2 cm, the spatial resolution was found to be 0.69 ± 0.05 (mean $\pm$ standard deviation) mm in the azimuth direction, 0.90 ± 0.03 mm in the elevation direction, and 0.84 ± 0.04 mm in the axial direction.

Figure 3(a) shows a photograph of the second gelatin phantom. The PA MAP image [Fig. 3(b)] only shows the black hair and the ink-dyed gelatin slab because of the PA wave generation by the light absorbing chromophores. In the pulse-echo US MAP image [Fig. 3(c)], two hairs are seen, but not the ink-dyed gelatin, because the acoustic impedance mismatch between the hair and the gelatin produces a strong US reflection, while the acoustic

impedance mismatch between the ink-dyed gelatin and surrounding gelatin is too small. The $1 \times 1 \times 1$ cm^3 volumetric PA and US images of the phantom are shown in Fig. 3(d) and 3(e). Figure 4(a) shows a photograph of the third gelatin phantom from top view. In the PA 3-D volumetric images [Fig. 4(b) and 4(c)], all three hairs at different depths were seen.

3.2 Rat SLN Mapping

To explore 3-D PA mapping of SLNs with methylene blue dye, we used the matrix array US probe to image the axillary region in a rat. A control PA MAP image was acquired before injection of methylene blue dye [Fig. 5(a)]. After injection, the blue dye accumulated in the SLNs by lymphatic drainage. Figure 5(b) and 5(c) shows the PA MAP images acquired at 5 and 30 min post-injection, respectively. The uptake of methylene blue in the rat SLN was clearly observed in the PA MAP images, which are all displayed with the same dynamic range. After dissection, the methylene blue-dyed SLN was visually identified as shown in the post mortem photograph [Fig. 5(d)].

The 3-D photoacoustic image from the rat SLN acquired at 30 min post-injection is rendered volumetrically in Fig. 5(e). The dynamics of the methylene blue accumulation in the SLN following injection for three rats is plotted in Fig. 5(f). A single-compartment model[21–24] was used to fit the methylene blue dye accumulation in the SLN.

$$\frac{dC}{dt} = k_{in}C_0 - k_{out}C, \qquad (1)$$

where C_0 and represent the methylene blue concentration in the bolus injection site (left forepaw pad) and the SLN, respectively; k_{in} and k_{out} are rate constants for the SLN's inward and outward transport of the blue dye; and t is the post-injection time. The solution to Eq. (1) is[23,24]

$$C = C_0 \frac{k_{in}}{k_{out}} (1 - e^{-k_{out}t}). \qquad (2)$$

The fitted curve, $C = 16.1(1 - e^{-0.142t}) + 4.03$, with an R^2 value of 0.785 is shown in Fig. 5(f). The mean PA signal amplitude enhancement at 30 min post-injection was ∼20 fold, compared to the pre-injection baseline signal amplitude.

4 Discussion and Conclusions

We have developed a 3-D PA and US imaging system comprised of a 2-D matrix array US probe and a modified clinical US system. Compared to previous PA imaging systems employing 2-D array US transducers,[12–14] this system provides
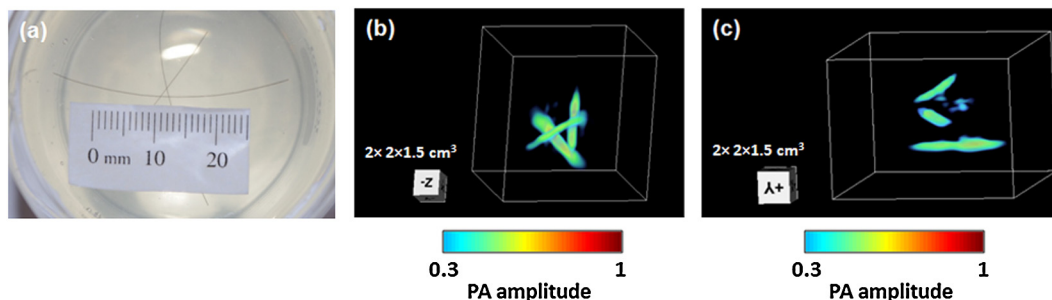

Fig. 4 (a) Photograph from top view of the gelatin phantom consisting of three black hairs placed 10, 15, and 20 mm deep. (b) 3-D PA image showing the black hairs from top view. (c) 3-D PA image showing the black hairs from side view. PA, photoacoustic.
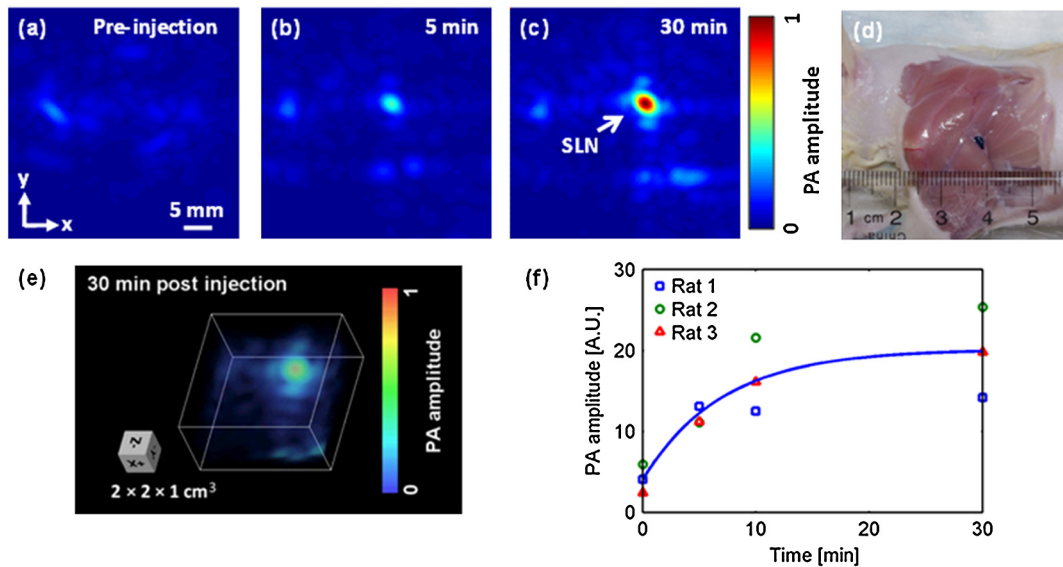
Fig. 5 (a) Control PA MAP image of rat axillary region acquired before the methylene blue dye injection. (b) PA MAP image taken 5 min post-injection showing the uptake of the blue dye in the SLN. (c) PA MAP image taken 30 min post-injection showing the PA signal enhancement in the SLN. (d) Post-mortem photograph of the rat taken after PA imaging and skin removal. (e) PA 3-D image taken 30 min after injection. (f) Plot of PA signal amplitudes from the SLNs (immediately after injection, at 5 min, 10 min, and 30 min post injection) fitted to a single compartment model $C = 16.1(1 - e^{-0.142t}) + 4.03$ with an R^2 value of 0.785 (C is the methylene blue concentration in the SLNs, and t is the post-injection time). PA, photoacoustic; and SLN, sentinel lymph node.

sub-millimeter spatial resolution, enables fast PA data acquisition, and incorporates real-time 3-D US imaging functionality of the commercial US scanner system. The current DAQ system acquires the PA data set for one volumetric frame in ~20 sec from 36 laser firings. To fully realize the potential of 3-D PA imaging, further system development will concentrate on improving the speed of data acquisition and utilizing fast Fourier transform (FFT) based 3-D reconstruction algorithm.[25]

Previous reports support the potential for PA SLNs mapping with a 2-D PA imaging system that employs a commercial linear array US probe.[6] Here, we present 3-D PA imaging of rat SLNs *in vivo* following accumulation of methylene blue dye. This new 3-D imaging system improves on earlier advancements of SLNs PA imaging by more efficiently and effectively acquiring 3-D images, and should facilitate the clinical application of PA imaging for SLNs mapping and image-guided SLN biopsy.

References

1. L. V. Wang, "Multiscale photoacoustic microscopy and computed tomography," *Nat. Photon.* **3**(9), 503–509 (2009).
2. C. Kim et al., "Deeply penetrating *in vivo* photoacoustic imaging using a clinical ultrasound array system," *Biomed. Opt. Express* **1**(1), 278–284 (2010).
3. R. A. Kruger et al., "Photoacoustic angiography of the breast," *Med. Phys.* **37**, 6096–6100 (2010).
4. H. Brecht et al., "Whole-body three-dimensional optoacoustic tomography system for small animals," *J. Biomed. Opt.* **14**(6), 064007 (2009).
5. A. Taruttis et al., "Real-time imaging of cardiovascular dynamics and circulating gold nanorods with multispectral optoacoustic tomography," *Opt. Express* **18**(19), 19592–19602 (2010).
6. T. N. Erpelding et al., "Sentinel lymph nodes in the rat: noninvasive photoacoustic and US imaging with a clinical US system," *Radiology* **256**(1), 102–110 (2010).
7. M. Li et al., "Simultaneous molecular and hypoxia imaging of brain tumors *in vivo* using spectroscopic photoacoustic tomography," *Proc. IEEE* **96**(3), 481–489 (2008).
8. X. Wang et al., "Noninvasive imaging of hemoglobin concentration and oxygenation in the rat brain using high-resolution photoacoustic tomography," *J. Biomed. Opt.* **11**(2), 024015 (2006).
9. E. W. Stein, K. Maslov, and L. V. Wang, "Noninvasive, *in vivo* imaging of blood-oxygenation dynamics within the mouse brain using photoacoustic microscopy," *J. Biomed. Opt.* **14**(2), 020502 (2009).
10. Y. Wang et al., "Fiber-laser-based photoacoustic microscopy and melanoma cell detection," *J. Biomed. Opt.* **16**(1), 011014 (2011).
11. L. Song, K. Maslov, and L. V. Wang, "Multifocal optical-resolution photoacoustic microscopy *in vivo*," *Opt. Lett.* **36**(7), 1236–1238 (2011).
12. S. Vaithilingam et al., "Three-dimensional photoacoustic imaging using a two-dimensional CMUT array," *IEEE Trans. Ultrason. Ferr.* **56**(11), 2411–2419 (2009).
13. A. Aguirre et al., "Coregistered three-dimensional ultrasound and photoacoustic imaging system for ovarian tissue characterization," *J. Biomed. Opt.* **14**(5), 054014 (2009).
14. S. Manohar et al., "Photoacoustic mammography laboratory prototype: imaging of breast tissue phantoms," *J. Biomed. Opt.* **9**(6), 1172–1181 (2004).
15. S. Manohar et al., "Initial results of *in vivo* non-invasive cancer imaging in the human breast using near-infrared photoacoustics," *Opt. Express* **15**(19), 12277–12285 (2007).
16. D. N. Krag et al., "Surgical resection and radiolocalization of the sentinel lymph node in breast cancer using a gamma probe," *Surg. Oncol.* **2**(6), 335–339 (1993).

17. K. K. Swenson et al., "Comparison of side effects between sentinel lymph node and axillary lymph node dissection for breast cancer" *Ann. Surg. Oncol.* **9**(8), 745–753 (2002).

18. K. H. Song et al., "Noninvasive photoacoustic identification of sentinel lymph nodes containing methylene blue *in vivo* in a rat model," *J. Biomed. Opt.* **13**(5), 054033 (2008).

19. M. Xu and L. V. Wang, "Universal back-projection algorithm for photoacoustic-computed tomography," *Phys. Rev. E* **71**(1), 016706 (2005).

20. American National Standard Institute Inc. (ANSI), ANSI z136.1-2007: American National Standard for the Safe Use of Lasers (ANSI, 2007).

21. M. A. Vieira-Coelho and P. Soares-Da-Silva, "Uptake and intracellular fate of l-DOPA in a human intestinal epithelial cell line: Caco-2," *Am. J. Physiol. Cell Physiol.* **275**(1), C104–C112 (1998).

22. R. G. Sheiman and A. Sitek, "Feasibility of measurement of pancreatic perfusion parameters with single-compartment kinetic model applied to dynamic contrast-enhanced CT images," *Radiology* **249**(3), 878–882 (2008).

23. H. A. Massaldi et al., "Improved method for estimating Ca uptake in vascular smooth muscle using compartmental analysis," *Am. J. Physiol. Regul. Integr. Comp. Physiol.* **259**(1), R172–R183 (1990).

24. V. Levin and C. S. Patlak, "A compartmental analysis of 24Na kinetics in rat cerebrum, sciatic nerve and cerebrospinal fluid," *J. Physiol.* **224**(3), 559–581 (1972).

25. B. E. Treeby and B. T. Cox, "k-Wave: MATLAB toolbox for the simulation and reconstruction of photoacoustic wave-fields," *J. Biomed. Opt.* **15**(2), 021314 (2010).